



ARTICLE

Open Access

Glass crystallization making red phosphor for high-power warm white lighting

Tao Hu¹, Lixin Ning², Yan Gao³, Jianwei Qiao¹, Enhai Song¹, Zitao Chen¹ , Yayun Zhou¹, Jing Wang¹ , Maxim S. Molokov^{5,6,7}, Xiaoxing Ke⁸, Zhiguo Xia¹ and Qinyuan Zhang¹

Abstract

Rapid development of solid-state lighting technology requires new materials with highly efficient and stable luminescence, and especially relies on blue light pumped red phosphors for improved light quality. Herein, we discovered an unprecedented red-emitting $\text{Mg}_2\text{Al}_4\text{Si}_5\text{O}_{18}:\text{Eu}^{2+}$ composite phosphor ($\lambda_{\text{ex}} = 450 \text{ nm}$, $\lambda_{\text{em}} = 620 \text{ nm}$) via the crystallization of $\text{MgO}-\text{Al}_2\text{O}_3-\text{SiO}_2$ aluminosilicate glass. Combined experimental measurement and first-principles calculations verify that Eu^{2+} dopants insert at the vacant channel of $\text{Mg}_2\text{Al}_4\text{Si}_5\text{O}_{18}$ crystal with six-fold coordination responsible for the peculiar red emission. Importantly, the resulting phosphor exhibits high internal/external quantum efficiency of 94.5/70.6%, and stable emission against thermal quenching, which reaches industry production. The maximum luminous flux and luminous efficiency of the constructed laser driven red emitting device reaches as high as 274 lm and 54 lm W^{-1} , respectively. The combinations of extraordinary optical properties coupled with economically favorable and innovative preparation method indicate, that the $\text{Mg}_2\text{Al}_4\text{Si}_5\text{O}_{18}:\text{Eu}^{2+}$ composite phosphor will provide a significant step towards the development of high-power solid-state lighting.

Introduction

Solid-state lighting (SSL) has advanced rapidly over the past decades, and will definitely dominate the future lighting market^{1–3}. The current standard architecture for SSL is the phosphor-converted light-emitting diode (pc-LED), where the blue LED chip is covered with one or more down-shifting phosphors dispersed in organic binder to produce composite white light^{4–7}. Despite those spectacular success in the pc-LED, the notorious “efficiency drop”, that is nonthermal drop in efficiency with increasing input power density^{8,9} precludes pc-LED operation in the fields, where high luminance and

luminous fluxes lighting source are required. Recently, laser diode (LD) driven SSL approach, whereby a focused laser beam illuminates a phosphor color converter, can generate luminance far exceeding the state-of-art LED source by factors of 2–10¹⁰. This way is particularly attractive for automotive headlamp, outdoor lighting, multimedia projectors, laser TVs and so on¹¹. However, the thermal shock of laser is extreme, making the traditional organic binders with poor physical and chemical stability undesired for LD applications¹². Accordingly, extensive efforts are preoccupied in the exploitation of new materials with highly efficient and stable luminescence, including single crystal phosphor, polycrystalline ceramic phosphor, and phosphor-in-glass (PiG)^{11,13–16}.

Although various types of bulk phosphors have been designed and constructed successfully so far, actually almost all reports are limited to Ce^{3+} -doped garnet-type yellow-emitting PiG/ceramic composite phosphors^{17,18}. Apparently, the high-power white lighting device based on “blue laser + yellow-emitting YAG: Ce^{3+} garnet” scheme is still flawed in application for the lack of red

Correspondence: Lixin Ning (ninglx@mail.ahnu.edu.cn) or

Zhiguo Xia (xiazg@scut.edu.cn) or Qinyuan Zhang (qyzhang@scut.edu.cn)

¹School of Physics and Optoelectronics, State Key Laboratory of Luminescent Materials and Devices and Guangdong Provincial Key Laboratory of Fiber Laser Materials and Applied Techniques, South China University of Technology, Guangzhou, Guangdong, China

²Anhui Key Laboratory of Optoelectric Materials Science and Technology, Key Laboratory of Functional Molecular Solids, Ministry of Education, Anhui Normal University, Wuhu, Anhui, China

Full list of author information is available at the end of the article

© The Author(s) 2021



Open Access This article is licensed under a Creative Commons Attribution 4.0 International License, which permits use, sharing, adaptation, distribution and reproduction in any medium or format, as long as you give appropriate credit to the original author(s) and the source, provide a link to the Creative Commons license, and indicate if changes were made. The images or other third party material in this article are included in the article's Creative Commons license, unless indicated otherwise in a credit line to the material. If material is not included in the article's Creative Commons license and your intended use is not permitted by statutory regulation or exceeds the permitted use, you will need to obtain permission directly from the copyright holder. To view a copy of this license, visit <http://creativecommons.org/licenses/by/4.0/>.

component, resulting a pale white light with high correlated color temperature (CCT >7500 K) and low color rendering index (CRI <75)^{19,20}. Thus, the discovery of efficient red-emitting bulk phosphor is essential. Concerning this case, particular efforts have been made to fabricate red-emitting CaAlSiN₃:Eu²⁺ PiG/ceramic composite^{21,22}, but few of them can fulfill the high demands generated by practice applications. The reasons are (1) CaAlSiN₃:Eu²⁺ phosphor unavoidably suffers from erosion when co-sintering it with glass frit at high-temperature¹⁷, which leads an inferior luminescent performance, viz., a lower quantum efficiency and stronger thermal emission quenching compared with the fresh CaAlSiN₃:Eu²⁺ phosphor powder. (2) The construction of ceramic is strictly constrained by high-pressure and high-vacuum conditions^{15,18,22}, and then such complex and economically unfavorable preparation processes hinder it from industrial production.

Crystallization of inorganic glass helps to realize new crystal formation and transformation for bulk composites with new functionalities in a pressureless, cost-effective, and scalable way in one step^{23–25}, as a typical example found in the in situ crystallization of a yellow-emitting Y₃Al₅O₁₂:Ce³⁺ nano-phosphor from Y₂O₃-Al₂O₃ glass²⁵. Despite that, formidable challenges still remained for this strategy to develop red-emitting Eu²⁺ activate bulk phosphor, and actually there is no report concerning this to the best of our knowledge. The major challenge mainly stems from the fact that one can hardly crystallize a host with suitable magnitude of centroid shift/crystal field splitting energy for the dopant, which can set the energy of 5*d* levels right at red electromagnetic spectrum region. Even so, encouraged by the large degree of freedom in glass composition design and the highly controllable crystallization processes, and thereby it enables us to intentionally manipulate spectroscopic features^{26,27}, breathtaking innovations of preparing red-emitting composite phosphor can be achieved prospectively.

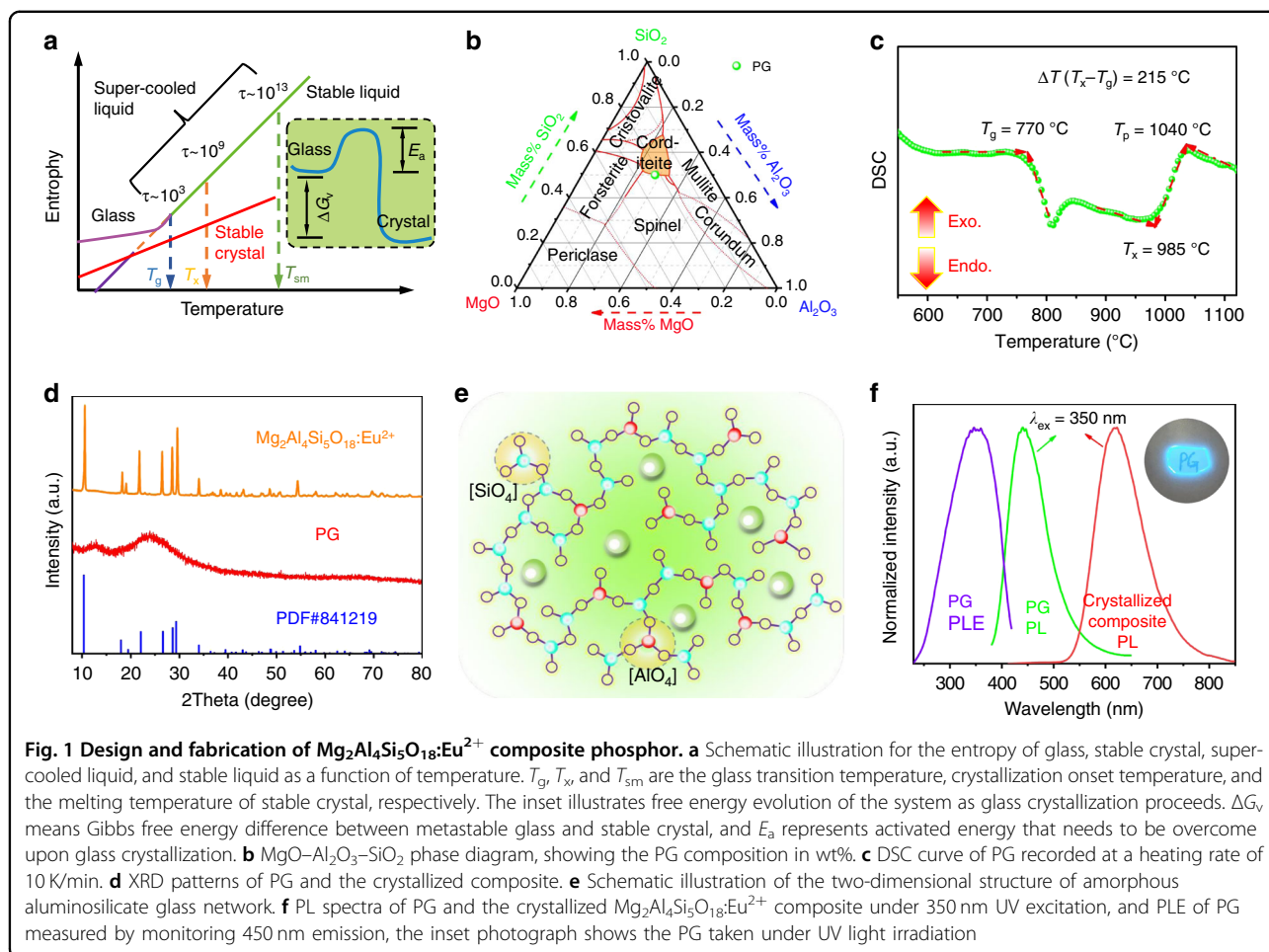
Herein, a glass crystallization engineering route for red-emitting phosphor is experimentally demonstrated for the first time. Specifically, by carefully designing the aluminosilicate glass matrix and conducting crystallization, we realize the fabrication of red-emitting Mg₂Al₄Si₅O₁₈:Eu²⁺ cordierite phosphor with near-unity photoluminescence quantum efficiency and excellent thermal stability. Noteworthy, cordierite (Mg₂Al₄Si₅O₁₈) is a famous material for its technologically important applications in integrated circuit substrates, electronic packaging, automotive catalyst, thermal insulation, and kiln furniture²⁸. It is also an excellent candidate for luminescent host accommodating various activators, particularly, by doping Eu²⁺ into Mg₂Al₄Si₅O₁₈. Several studies showed Mg₂Al₄Si₅O₁₈:Eu²⁺ exhibited single-band blue emission^{29–31}, and recently dual-band emission with strong

blue and weak red luminescence was also reported³². However, it is a challenge to address the Eu²⁺ luminescence and its crystallographic occupancy, and more importantly, one cannot prepare the important red-emitting phosphors pumped by blue light in this system. Herein, novel red Mg₂Al₄Si₅O₁₈:Eu²⁺ bulk composite has been reported, and combined experimental and theoretical investigations are performed to uncover the relationships between crystallographic structures and luminescence properties. Moreover, the laser driven red-emitting device constructed using Mg₂Al₄Si₅O₁₈:Eu²⁺ exhibits a high luminous flux and luminous efficiency, demonstrating it can serve as efficient color converter for high-power warm white-lighting application. Indeed, a high-quality warm white-lighting with a low CCT (4146 K) and excellent CRI ($R_a = 85.2$, $R_g = 64.5$) is also fulfilled.

Results and discussion

Fabrication of red-emitting Mg₂Al₄Si₅O₁₈:Eu²⁺ composite via glass crystallization

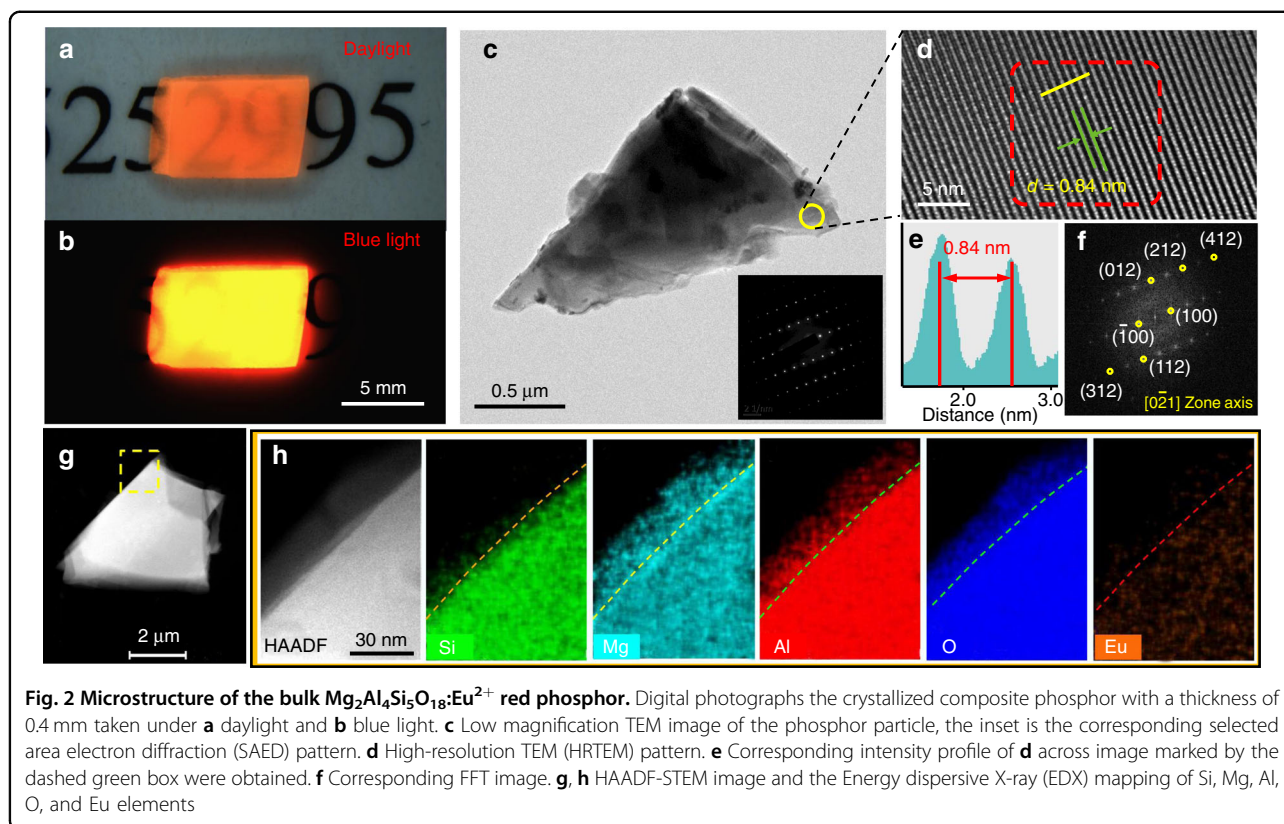
Glass is a thermodynamically metastable (non-equilibrium) solid. After it is heat-treated for a sufficiently long time at higher than glass transition temperature T_g , it will enter into super-cooled state, and then glass structure relaxation could occur, leading to the movement/diffusion of multiple structural building blocks simultaneously or atomic rearrangements orderly. Consequently, precipitating thermodynamically stable (equilibrium) crystal occurred with reducing the free energy of the system, as schematically depicted in Fig. 1a and inset 1a³³. Theoretically, by carefully selecting glass system and designing chemical compositions (i.e., by controlling over the topological structure of glass network, especially the medium-, or short-range structural arrangement), one may intentionally manipulate nucleation/growth of crystalline within glass as desired. As demonstrated by the typical example of MgO–Al₂O₃–SiO₂ ternary phase diagram³⁴ (Fig. 1b), the tailoring of those ternary compositions could selectively crystallize several types of crystallines of spinel, mullite, forsterite, and cordierite, which are all well-known hosts to accommodate optical-active impurities. Herein, aluminosilicate precursor glass (PG) with the nominal chemical composition of 2MgO–Al₂O₃–3SiO₂, which is at the boundary between cordierite (chemical formula of Mg₂Al₄Si₅O₁₈) and spinel (Fig. 1b), was specially designed and prepared via melt-quenching method. Broad XRD scattering at about $2\theta = 25^\circ$ together without any diffraction peaks confirm the amorphous structure of network of the as-quenched PG. EDS examination shows the homogeneously distribution of elements and its chemical compositions (Fig. S1), with the atom ratio of Mg/Al/Si in accordance with the nominal compositions (Table S1). The thermodynamic



parameters of the PG were recorded by DSC thermogram (Fig. 1c), where the glass transition temperature T_g , the onset of crystallization temperature T_x , and maximum crystallization temperature T_p are determined to be 770, 985, and 1040 °C, respectively. The temperature difference ΔT ($T_x - T_g$) is calculated to be 215 °C, and such a big value is due to the fact that the glass network structure constructed by Al_2O_3 and SiO_2 is rigid and thermally stable. Specifically, the glass structure relaxation and crystallization were processed via a heat-treatment at 1120 °C, which is slightly higher than T_p . As shown in Fig. 1d, after annealing, the glass hump disappeared completely and the sharp diffraction peaks are indexed to $\text{Mg}_2\text{Al}_4\text{Si}_5\text{O}_{18}$ (PDF#841219) phase, manifesting the high crystallinity and the successful preparation of $\text{Mg}_2\text{Al}_4\text{Si}_5\text{O}_{18}$ bulk composite. The precipitation of $\text{Mg}_2\text{Al}_4\text{Si}_5\text{O}_{18}$ crystal matches well with $\text{MgO}-\text{Al}_2\text{O}_3-\text{SiO}_2$ ternary phase diagram prediction (Fig. 1b). $\text{Mg}_2\text{Al}_4\text{Si}_5\text{O}_{18}$ is known to crystallize in two polymorphs, high-temperature hexagonal structure and low-temperature orthorhombic. To clarify the structure and the phase purity, Rietveld refinement was conducted with the high-

quality synchrotron XRD data by using TOPAS 4.2³⁵, as shown in Fig. S2. Almost all peaks were indexed by hexagonal cell ($P6/mcc$) with parameters close to $\text{Mg}_2\text{Al}_4\text{Si}_5\text{O}_{18}$, except for several weak diffraction peaks of forsterite impurity phase. The amount of $\text{Mg}_2\text{Al}_4\text{Si}_5\text{O}_{18}:\text{Eu}^{2+}$ phase, determined by Rietveld refinement, is 95.8% by weight. Refinement taking hexagonal structure as starting model was stable and gave low R -factors (Table S2). Coordinates of atoms and main bond lengths are listed in Tables S3 and S4, respectively.

Due to the sensitivity of Fourier-transform infrared (FTIR) spectra to short-range interactions, the FTIR spectra were measured, aiming to gain knowledge of the network topology evolution from glass to hexagonal $\text{Mg}_2\text{Al}_4\text{Si}_5\text{O}_{18}$ crystal. As shown in Fig. S3, the PG exhibits three absorption bands in the region of 400–1400 cm^{-1} . The intense bands in 800–1200 cm^{-1} are assigned to the stretching vibrations of the $[\text{SiO}_4]$ tetrahedron with a different number of bridging oxygen atoms (1150 cm^{-1} for Q^4 , 1090 cm^{-1} for Q^3 , and 980 cm^{-1} for Si-O-[NBO, non-bridging oxygen] (Q^3) per $[\text{SiO}_4]$ tetrahedron). The next intense band between

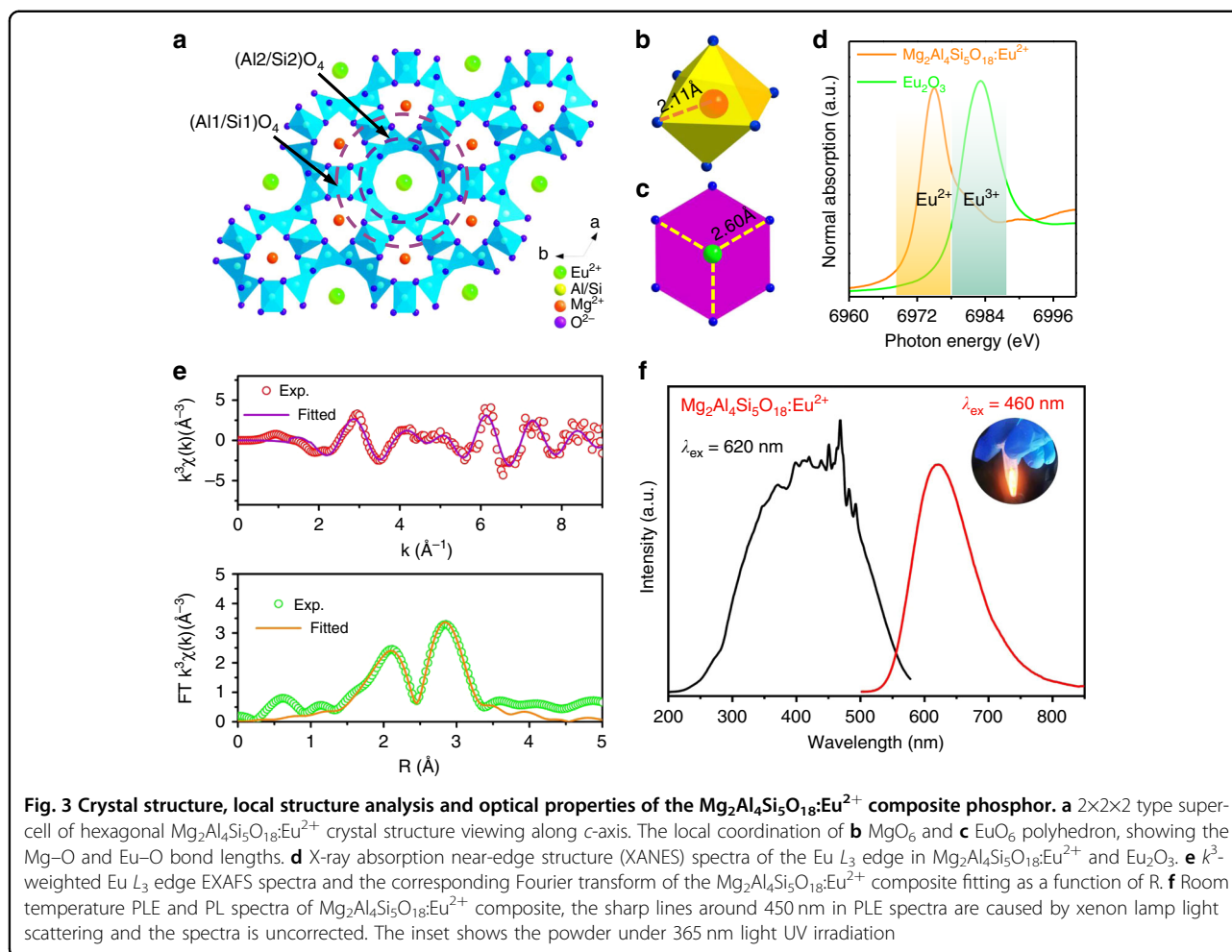


400 and 600 cm^{-1} are due to bending vibrations of Si–O–Si and Si–O–Al linkages, and the band in the $600\text{--}800\text{ cm}^{-1}$ region relates to the stretching vibrations of the Al–O bonds with aluminum ions in four-fold coordination³⁶. All those indicate that the glass network essentially consists of $[\text{AlO}_4]$ and $[\text{SiO}_4]$ tetrahedrons (Fig. 1e). The small Mg^{2+} cation acts as network modifier to balance the negative charges of either non-bridging oxygen ions or tetrahedral structure unites. The glass crystallization results in the characteristic modification of FTIR with its profile approximately coinciding with that of the PG, implying that the structure of the PG and crystal in the short-range scale are topologically identical. As a result of the ordered reconstruction of $[\text{AlO}_4]$ and $[\text{SiO}_4]$ tetrahedrons, the absorption peak for the composite becomes split and rather sharp, and the quite intense band at $\sim 575\text{ cm}^{-1}$ is the typical vibration of the 6-membered aluminosilicate rings in $\text{Mg}_2\text{Al}_4\text{Si}_5\text{O}_{18}$ crystal³⁷. It is believed that heterogeneity structure on the nanometer scale of the PG plays a decisive role in precipitating $\text{Mg}_2\text{Al}_4\text{Si}_5\text{O}_{18}$ crystal. The structure and chemical composition of nano-scale heterogeneity part might be closely related to the initial crystalline phase (topological crystalline-like ordering exists)³³, which favors precipitating $\text{Mg}_2\text{Al}_4\text{Si}_5\text{O}_{18}$ when heat energies are being supplied.

In addition to phase transformation engineering, chemical surrounding for the optical-active dopant was tailored simultaneously, resulting in intriguing optical properties. As exhibited in Fig. 1f and inset of Fig. 1f, upon introducing Eu^{2+} dopant into the as-made PG, it exhibits bright blue light at $\sim 450\text{ nm}$. Interestingly, blue emission is almost vanished and red emission is dominated for the final crystallized composite, suggesting the glass relaxation and crystallization energetically drives the Eu^{2+} dopants from aluminosilicate glass towards the precipitated $\text{Mg}_2\text{Al}_4\text{Si}_5\text{O}_{18}$ crystalline lattice with a more prominent crystal field splitting, and the completely vanishment of blue emission also indicates the high doping efficiency.

Microstructure analysis

Figure 2a, b exhibit the photographs of the bulk $\text{Mg}_2\text{Al}_4\text{Si}_5\text{O}_{18}:\text{Eu}^{2+}$ composite phosphor taking under daylight and 450 nm blue light excitation. The apparent body color is orange red vividly, and bright red luminescence is observed upon blue light irradiation (Fig. 2a). It is also at a high level of densification and no pores or voids could be observed at various magnification scales (Fig. S4). TEM image and the corresponding SAED pattern (Fig. 2c and inset of Fig. 2c) demonstrate the single crystalline feature with high crystallinity of microparticle. The high-resolution TEM (HRTEM) pattern shows the



distinct lattice fringes (Fig. 2d). A typical interplanar spacing of 0.84 nm is matching well with the (1 0 0) plane of hexagonal $\text{Mg}_2\text{Al}_4\text{Si}_5\text{O}_{18}$ crystal, according to the fast Fourier transform (FFT) image viewing along [0-21] zone axis (Fig. 2e, f). There are no lattice fringes at the edge of the crystal (the region surrounded by yellow dotted line in Fig. S5), suggesting it is the tiny remaining glassy phase. High-angle annular dark-field scanning TEM (HAADF-STEM) observations and the corresponding element mappings (Fig. 2g, h) were also carried out to characterize the microstructure. As observed in element mappings, the Mg, Al, Si, and O are homogeneously distributed over the crystal, whereas the Mg, Al, and O are rich over the glassy phase. The absence of Si in the remaining glassy suggests the almost totally depletion of Si in the process of $\text{Mg}_2\text{Al}_4\text{Si}_5\text{O}_{18}$ crystallize propagation.

Site occupancy and optical properties

Figure 3a depicts the crystal structure of hexagonal $\text{Mg}_2\text{Al}_4\text{Si}_5\text{O}_{18}:\text{Eu}^{2+}$. The Al and Si atoms are disorderly distributed over two sets of tetrahedral sites to form (Al1/Si1) O_4

and (Al2/Si2) O_4 tetrahedrons. The Mg atoms are surrounded by the (Al/Si) O_6 -type 6-membered rings, and are six-fold coordinated to form MgO_6 octahedrons (Fig. 3b). Comparing the ionic radius of Eu^{2+} ($r_{6\text{-coord.}} = 1.17 \text{ \AA}$) with that of Mg^{2+} ($r_{6\text{-coord.}} = 0.72 \text{ \AA}$) suggests that it is unlikely for Eu^{2+} to replace Mg^{2+} because their radius difference is as high as $\sim 62.5\%$, which is far beyond the limits of the Hume-Rothery rules for atomic substitution³⁸.

There are large vacant channels running parallel to the c -axis in the $\text{Mg}_2\text{Al}_4\text{Si}_5\text{O}_{18}$ (Fig. S6), and it has been reported that the channels have the capability to accommodate a variety of cation ions³⁹. Therefore, one can easily speculate that the Eu^{2+} ions inserted at the channel sites. Figure S7a, b demonstrate the two kinds of strikingly different channel sites in the host, namely, $z = 0.0$ or 0.5 site with six-fold coordinated planar oxygen, another is $z = 0.25$ or 0.75 with 12-fold coordinated oxygen³². To understand the site occupation, DFT calculations were conducted to evaluate the relative occurrence probabilities of Eu^{2+} substitutions at various sites. Before

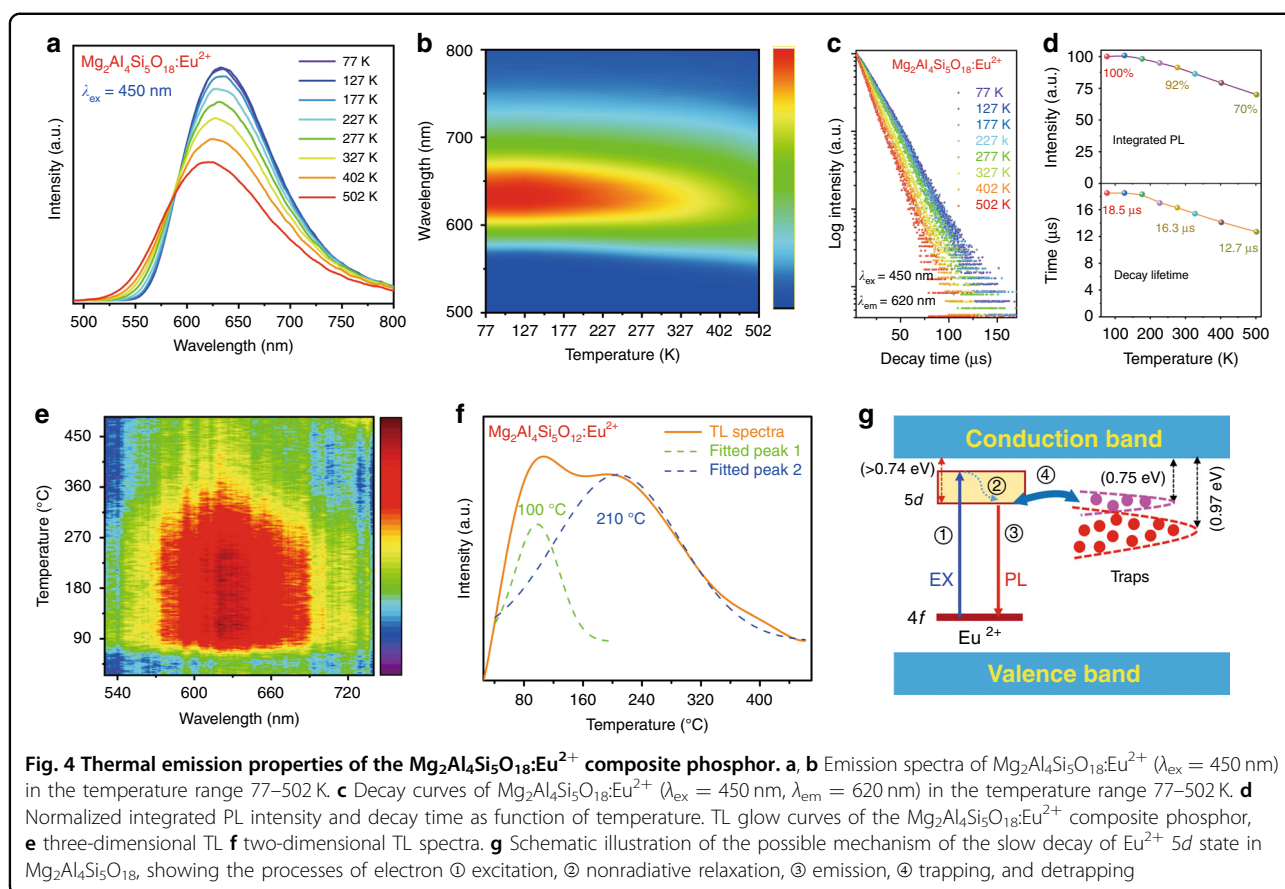
doing so, the occupational disorder at Al1/Si1 (6f) and Al2/Si2 (12l) sites needs to be modeled first. In accordance with the Rietveld results (Table S3), the occupancy ratios at the two sites were approximated by Al1/Si1 = 5/1 and Al2/Si2 = 1/3. The resultant atomic composition is consistent with the chemical formula. With this approximation, there are totally 1320 different atomic configurations of the unit cell, which when the crystal symmetry is taken into account⁴⁰, reduces to 57 crystallographically independent configurations that are necessary for calculations. The relative occurrence probability (P_i) of each configuration with multiplicity i was evaluated with $P_i = \frac{1}{Z_{\text{tot}}} \Omega_i \exp(-\frac{E_i}{kT})$ ($i = 1, \dots, 57$), where Z_{tot} is the partition function, E_i is the relative DFT total energy, k is the Boltzmann constant, and T is the synthesis temperature of the material. It was found that five distinct configurations dominate the configurational ensemble, with the relative occurrence probabilities $P = 0.624, 0.132, 0.076, 0.074$, and 0.062 , respectively. For the other inequivalent configurations, each $P < 0.006$. Based on this, the undoped unit cells with these five configurations were employed for subsequent investigation of Eu^{2+} site occupations.

For $\text{Mg}_2\text{Al}_4\text{Si}_5\text{O}_{18}:\text{Eu}^{2+}$, we have considered two kinds of Eu^{2+} substitutions, that is, isovalent substitution at the host Mg^{2+} site (Eu_{Mg}), and occupations within the vacant channel (Eu_{vac}) at $z = 0.0, 0.25, 0.5$, and 0.75 with a Mg vacancy (V_{Mg}) or two antisite defects (2Al_{Si}) as the charge compensator. The DFT calculations revealed that the defect formation energies of Eu_{Mg} and $\text{Eu}_{\text{vac}}-V_{\text{Mg}}$ are at least by 2.5 eV higher than the most stable $\text{Eu}_{\text{vac}}-2\text{Al}_{\text{Si}}$ complexes. This means that Eu_{Mg} and $\text{Eu}_{\text{vac}}-V_{\text{Mg}}$ are unlikely to occur compared to $\text{Eu}_{\text{vac}}-2\text{Al}_{\text{Si}}$, and will thus be discarded in the following discussion. For Eu_{vac} at each site within the vacant channel, there are 45 $\text{Al}_{\text{Si}}-\text{Al}_{\text{Si}}$ combinations in a given unit cell. As such, for the five most probable atomic configurations of unit cell each with four substituted sites (z), a total of 900 Eu^{2+} -incorporated different cells have been calculated by DFT to explore the site preference of Eu^{2+} within the vacant channel. The results show that Eu^{2+} locations at $z = 0.25$ and 0.75 sites are unstable in that the Eu^{2+} initially positioned at these sites would relax into $z = 0.0$ or 0.5 sites during DFT geometry optimization. The most stable configurations (to within 100 meV) have Eu^{2+} located at $z = 0.0$ or 0.5 site, surrounded by six O in a quasi-planar structure in the first coordination shell and $2\text{Al} + 4\text{Si}$ or $3\text{Al} + 3\text{Si}$ atoms randomly distributed in the second coordination shell, which is in line with the occupational disorder of Al/Si sites. Therefore, DFT calculations predict that most Eu^{2+} ions are located at $z = 0.0$ or 0.5 sites with six-fold coordination within the vacant channel (Fig. 3a, c).

To experimentally determine the location of Eu and its valance state, extended X-ray absorption fine structure (EXAFS) at the Eu L_3 edge was measured. Figure 3d shows

the Eu L_3 edge X-ray absorption near-edge structure (XANES) spectra of the composite phosphor and Eu_2O_3 . The absorption energy at about 6975 and 6982 eV are attributed to $2p_{3/2} \rightarrow 5d$ transitions of Eu^{2+} and Eu^{3+} , respectively. The absence of 6982 eV peak for the composite suggests that the valance state of Eu in the $\text{Mg}_2\text{Al}_4\text{Si}_5\text{O}_{18}$ is in divalent oxidation state, which is also beneficial for achieving high efficiency luminescence. The EXAFS spectra were processed in Athena (version 0.9.25) for background, pre-edge line, and post-edge line calibrations. Then Fourier transformed fitting was carried out in Artemis (version 0.9.25). The k^3 weighting, k -range of $3-9 \text{ \AA}^{-1}$ and R range of $1-4 \text{ \AA}$ were used for the fitting. The four structure parameters, including coordination number (CN), bond length (R), Debye-Waller factor (σ^2), and E_0 shift (ΔE_0) were fitted without anyone was fixed, constrained, or correlated. The reciprocal space k^3 weighting EXAFS and the corresponding Fourier transformed spectra are shown in Fig. 3e. The fitted structure parameters are presented in Table S5. The spectra were well fitted (R factor = 0.006), with the fitted CN in the first coordinated shell is 6.5 ± 1.6 , and R for Eu-O bond is $2.60 \pm 0.03 \text{ \AA}$. This strongly supports that Eu^{2+} incorporates in the $z = 0.0$ or 0.5 channel sites as the fitted parameters are consistent well with that of the non-doped $\text{Mg}_2\text{Al}_4\text{Si}_5\text{O}_{18}$ (the diameter of the channel is $\sim 5.6 \text{ \AA}$, and those sites are six-fold coordination), in line with the DFT calculations discussed above. Indeed, cordierite is an incredible phosphor host, and the blue emission in $\text{Mg}_2\text{Al}_4\text{Si}_5\text{O}_{18}:\text{Eu}^{2+}$ was also reported previously, and the origin of the Eu^{2+} occupation is still a controversial issue^{29,30}. As such, one can still expect future work to address some important findings on this topic.

Figure 3f displays the photoluminescence excitation and emission spectra of $\text{Mg}_2\text{Al}_4\text{Si}_5\text{O}_{18}:\text{Eu}^{2+}$ composite phosphor measured at room temperature. It exhibits bright red-light emission under near UV light irradiation (inset of Fig. 3f). Under 450 nm blue light excitation, the PL spectrum consists a broad band emission with the maximum peak at $\sim 620 \text{ nm}$, ascribed to parity-allowed electric dipole Eu^{2+} : $4f^65d \rightarrow 4f^7(^8S_{7/2})$ transition. The excitation spectra by monitoring 620 nm emission exhibits a broad band with the maximum peak at around 450 nm; therefore, the phosphor is blue light highly excitable. Noteworthy, the realization of Eu^{2+} red emission in oxide-based host is known a challenge task. Recently, Stefańska et al. observed the red emission in $\text{Mg}_2\text{Al}_4\text{Si}_5\text{O}_{18}:\text{Eu}^{2+}$ phosphor powder³², which was, however, accompanied with the strong blue emission. PL decay of the $4f^65d$ state displays a nearly single exponent decay (Fig. S8), and time-resolved PL spectra shows an insignificant variation of emission profile at as time prolongs from 7 to 56 μs (Fig. S9), suggesting a homogeneous crystal field environment around Eu^{2+} in $\text{Mg}_2\text{Al}_4\text{Si}_5\text{O}_{18}$ lattice. The derived



luminescence decay time is $15.4 \mu\text{s}$, which is unexpectedly long compared to those (about $1.0 \pm 0.5 \mu\text{s}$ ⁴¹). The origin of this slow decay will be discussed later. Under 450 nm blue light excitation, the composite phosphor exhibits a high internal/external quantum efficiency of 94.5/70.6% (Fig. S10), guaranteeing its practical application.

As is known, the thermal shock of laser during the application is extreme, with the laser pump power of even a few watts into sub-millimeter spot can easily raise local temperature well into hundreds of degrees Celsius. Therefore, thermally stable properties are necessarily required in laser applications. Temperature-dependent XRD patterns (Fig. S11) verify the phase and physico-chemical stability of the as-fabricated $\text{Mg}_2\text{Al}_4\text{Si}_5\text{O}_{18}:\text{Eu}^{2+}$ composite. The emission spectra ($\lambda_{\text{ex}} = 450$ nm) in Fig. 4a, b are gradually blue-shifted and broadened (Fig. S12) with increasing temperature, as commonly observed for Eu^{2+} emission. The blue shift is caused by lattice thermal expansion (Fig. S13), which increases the Eu–O distance and thus results in a smaller crystal field splitting and a decreased covalency. The spectrum broadening is essentially due to the enhanced electron–phonon interaction at high temperature, inducing the electron thermally populate to higher vibrational levels. The PL decay curves at various temperature are close to single-

exponential (Fig. 4c). The composite exhibits excellent thermal stable luminescence; the integrated PL intensity at 423 K (150 °C) remains $\sim 78\%$ of that at 70 K (Fig. 4d). The quenching temperature ($T_{0.5}$), namely, the temperature at which the emission intensity (or decay time) drops to 50% of the low-temperature value, is higher than 500 K (Fig. 4d), from which the activation energy (E_a) for thermal quenching can be estimated to be larger than 0.74 eV⁴². The thermal conductivity is measured to be $\sim 2.2 \text{ W m}^{-1} \text{ K}^{-1}$, larger than that of the organic binder of $\sim 0.1\text{--}0.2 \text{ W m}^{-1} \text{ K}^{-1}$ ¹² and the co-sintered PiG of $\sim 1 \text{ W m}^{-1} \text{ K}^{-1}$ ¹³. In addition, thanks to the robust of inorganic aluminosilicate matrices, the phosphor also shows good anti-moisture properties (Fig. S14). All those results indicate the $\text{Mg}_2\text{Al}_4\text{Si}_5\text{O}_{18}:\text{Eu}^{2+}$ phosphor is robust enough to withstand the thermal shock of blue LD and humidity during the applications.

Figure 4e shows the three-dimensional thermoluminescence (TL) spectra of $\text{Mg}_2\text{Al}_4\text{Si}_5\text{O}_{18}:\text{Eu}^{2+}$ composite phosphor. The TL emission peaked at ~ 620 nm, confirming that the defect-trapped charge carriers were thermally released to generate excited Eu^{2+} giving rise to the red emission. The two-dimensional TL spectrum covers a wide temperature range from 30 to 500 °C (Fig. 4f), indicating a continuous distribution of defect trap

depth. The spectrum can be fitted by two Gaussian bands peaking at 100 and 210 °C, for which the trap depths (E_T) can be estimated to be 0.76 and 0.97 eV, respectively, on the basis of the approximate equation $E_T = T/500$, where the temperature T is in units of kelvin. These defects could be oxygen vacancies, which have been commonly observed in oxides synthesized in reducing atmosphere and confirmed to be responsible for thermal behavior of Eu^{2+} luminescence⁴³.

As mentioned earlier, the long decay time (15.4 μs) of Eu^{2+} -related red emission is striking. Dorenbos has proposed the requirements to be met for Eu^{2+} -related anomalous emission, namely, a much larger Stokes shift, a broad emission band, and a longer decay time than the normal Eu^{2+} emission⁴⁴. This anomalous emission originates from the close proximity between the excited Eu^{2+} $5d$ emitting level and the bottom of the host conduction band. Upon Eu^{2+} $4f \rightarrow 5d$ excitation, the electron in the $5d$ level delocalizes into the host band state generating a Eu^{3+} -trapped excitonic state, from which the transition to the Eu^{2+} $4f$ ground state leads to a strongly red-shifted emission compared to the normal $5d \rightarrow 4f$ emission. In the present case of $\text{Mg}_2\text{Al}_4\text{Si}_5\text{O}_{18}:\text{Eu}^{2+}$, however, the red emission is considered to be normal because (1) the Stokes shift (3700 cm^{-1}) is not large, (2) the emission band (FWHM = 2700 cm^{-1}) is not broad, and (3) the emitting level is well below the host conduction band ($E_a > 0.74\text{ eV}$). If so, what is the cause for the surprising long-decay of the red $5d \rightarrow 4f$ emission?

In $\text{Mg}_2\text{Al}_4\text{Si}_5\text{O}_{18}:\text{Eu}^{2+}$, the TL measurement revealed a distribution of defect trap levels with main peaks at 0.76 and 0.97 eV below the host conduction band edge (Fig. 4g). The energy positions of these defect levels are close to that of Eu^{2+} $5d$ emitting level ($>0.74\text{ eV}$ below the host conduction band edge). At room temperature, the electrons trapped at these defect levels can be thermally activated to release into Eu^{2+} $5d$ levels, which results in $5d \rightarrow 4f$ emission with a long decay time. At lower temperature the luminescence decay would be longer in view of the thermally activated electron transfer, consistent with experimental observations (Fig. 4c). A schematic representation of the luminescence mechanism is depicted in Fig. 4g. Upon 450 nm irradiation, Eu^{2+} is excited from the $4f$ ground state to higher $5d$ levels (process 1), which then relaxes nonradiatively to the lowest $5d$ level (process 2). From this excited level, the $5d$ electron can return back to the $4f$ ground state by emitting a red photon (process 3), or transfer to nearby electron-trapping defects by direct tunneling (process 4) due the close proximity between the Eu^{2+} $5d$ and defect levels. During the decay-time measurement of the $5d \rightarrow 4f$ emission, the electron trapped at the defects will transfer back (process 4) to the emitting $5d$ level, leading to luminescence decay time much longer than the normal case.

Demonstration of application for LD lighting

The blue laser driven red lighting device was constructed by coupling the $\text{Mg}_2\text{Al}_4\text{Si}_5\text{O}_{18}:\text{Eu}^{2+}$ composite with 445 nm blue laser diode aiming to evaluate its potential application for high power lighting. As plots in Fig. 5a, b, the emission intensity of the composite increases monotonously as the laser power density increases from 0.25 to 3.25 W mm^{-2} , beyond which luminescence saturation occurs. The maximum luminous flux and luminous efficiency achieved for $\text{Mg}_2\text{Al}_4\text{Si}_5\text{O}_{18}:\text{Eu}^{2+}$ composite phosphor is $\sim 274\text{ lm}$ and 54 lm W^{-1} , respectively. The time-dependent emission spectra under a fixed power density of 1.5 W mm^{-2} (Fig. S15), and the corresponding luminous flux (Fig. 5c) demonstrate the composite phosphor is stable enough in practice application. We also made a performance comparison between our composite and the previously reported red $\text{CaAlSiN}_3:\text{Eu}^{2+}$ ceramic synthesized by using the state-of-art red $\text{CaAlSiN}_3:\text{Eu}^{2+}$ phosphor. As shown in Fig. 5d, the maximum luminous flux and luminous efficiency achieved for $\text{CaAlSiN}_3:\text{Eu}^{2+}$ ceramic is about 203 lm and 41 lm W^{-1} ²², which is inferior to our reported photoelectric properties and actually the photoelectric properties realized in $\text{Mg}_2\text{Al}_4\text{Si}_5\text{O}_{18}:\text{Eu}^{2+}$ composite is almost the highest rank among red bulk phosphors. Anyway, all those results suggest that the $\text{Mg}_2\text{Al}_4\text{Si}_5\text{O}_{18}:\text{Eu}^{2+}$ holds potential for addressing the lack of commercially available all-inorganic red-emitting bulk color converter.

Finally, we constructed the blue laser driven white lighting device by using a stack package configuration, in which the commercial $\text{LuAG}:\text{Ce}^{3+}$ ceramic serving as a green color converter is stack packed with red $\text{Mg}_2\text{Al}_4\text{Si}_5\text{O}_{18}:\text{Eu}^{2+}$ to form white light (Fig. 6a, b). Figure 6c demonstrates the emission spectra of the white lighting device operating under the incident power density of 0.25 W mm^{-2} . The device exhibits a low correlated color temperature (CCT) of 4146 K, high color render index ($R_a = 85.2$, $R_9 = 64.5$), and CIE chromaticity coordinates of (0.364, 0.333), which is much better than the properties of the $\text{YAG}:\text{Ce}^{3+}$ -based laser driven white lighting featuring a high CCT ($>7500\text{ K}$) and a low R_a (<75)¹⁵. The incident power density dependent emission spectra, luminous flux and luminous efficiency are presented in Fig. 6d, e and Table S6. With the increment of pumping power density from 0.25 to 4 W mm^{-2} , the output of the white light is get enhanced gradually, and the CIE chromaticity coordinates at various power densities are near at Planckian locus curve (Fig. 6f). The maximum luminous flux (480 lm) and luminous efficiency (94.1 lm W^{-1}) realized in our white lighting device is relatively low compared with that of the $\text{YAG}:\text{Ce}^{3+}$ -based laser driven white lighting device, partly due to the output of green light is blocked by the red composite. We think there is a large space to improve it via carefully design packing

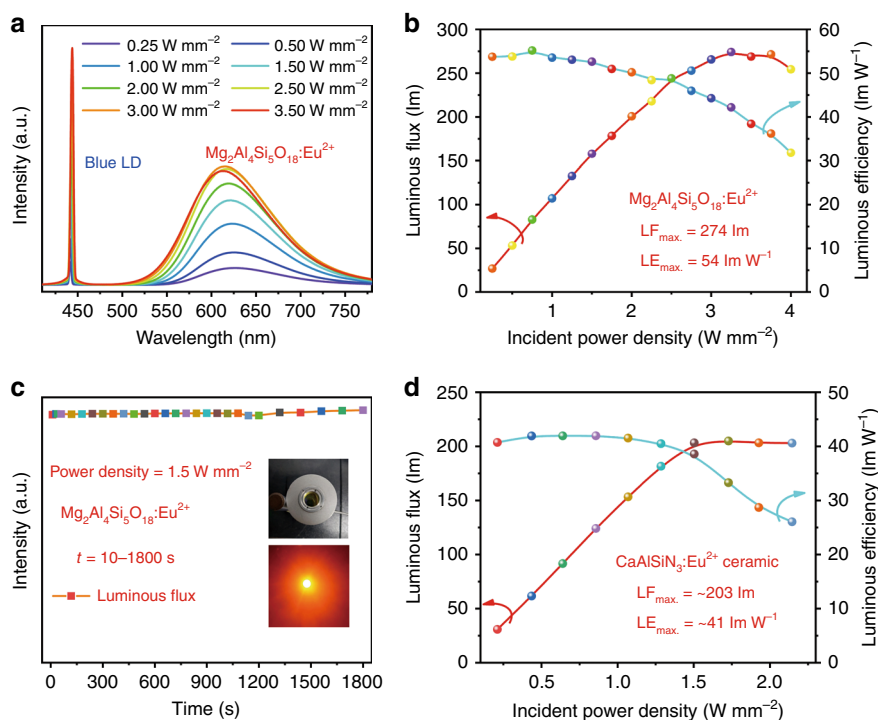


Fig. 5 Photoelectric properties of the LD driven red-emitting device constructed by using $\text{Mg}_2\text{Al}_4\text{Si}_5\text{O}_{18}:\text{Eu}^{2+}$ phosphor. The power density-dependent **a** luminescent spectra **b** luminous flux and luminous efficiency of $\text{Mg}_2\text{Al}_4\text{Si}_5\text{O}_{18}:\text{Eu}^{2+}$ composite under the excitation of 445 nm blue laser. **c** Time-dependent luminous flux of the composite at a fixed incident power density of 1.5 W mm^{-2} , the inset show the photograph of red LD device. **d** The incident power density-dependent luminous flux and luminous efficiency of the $\text{CaAlSiN}_3:\text{Eu}^{2+}$ ceramic²²

configuration or material design, for example, by further optimization of the transparency of the red composite, or even fabrication of $\text{LuAG}:\text{Ce}^{3+}/\text{Mg}_2\text{Al}_4\text{Si}_5\text{O}_{18}:\text{Eu}^{2+}$ binary composite.

Conclusions

In summary, we report a facile elaboration of new type of red-emitting $\text{Mg}_2\text{Al}_4\text{Si}_5\text{O}_{18}:\text{Eu}^{2+}$ composite phosphor based on glass relaxation and crystallization of a composition specially designed aluminosilicate glass at ambient conditions. The optical properties realized here are especially surprising, because red phosphor exhibits near unity luminescence efficiency and stable emission against temperature, which enables it readily meets the high-power laser driven lighting applications. Our demonstration represents the first proof-of-principle glass crystallization of red-emitting composite phosphor, and we believe that it will provide a great step toward the advancement of new materials discovery of the solid-state lighting technology for the new photonic applications.

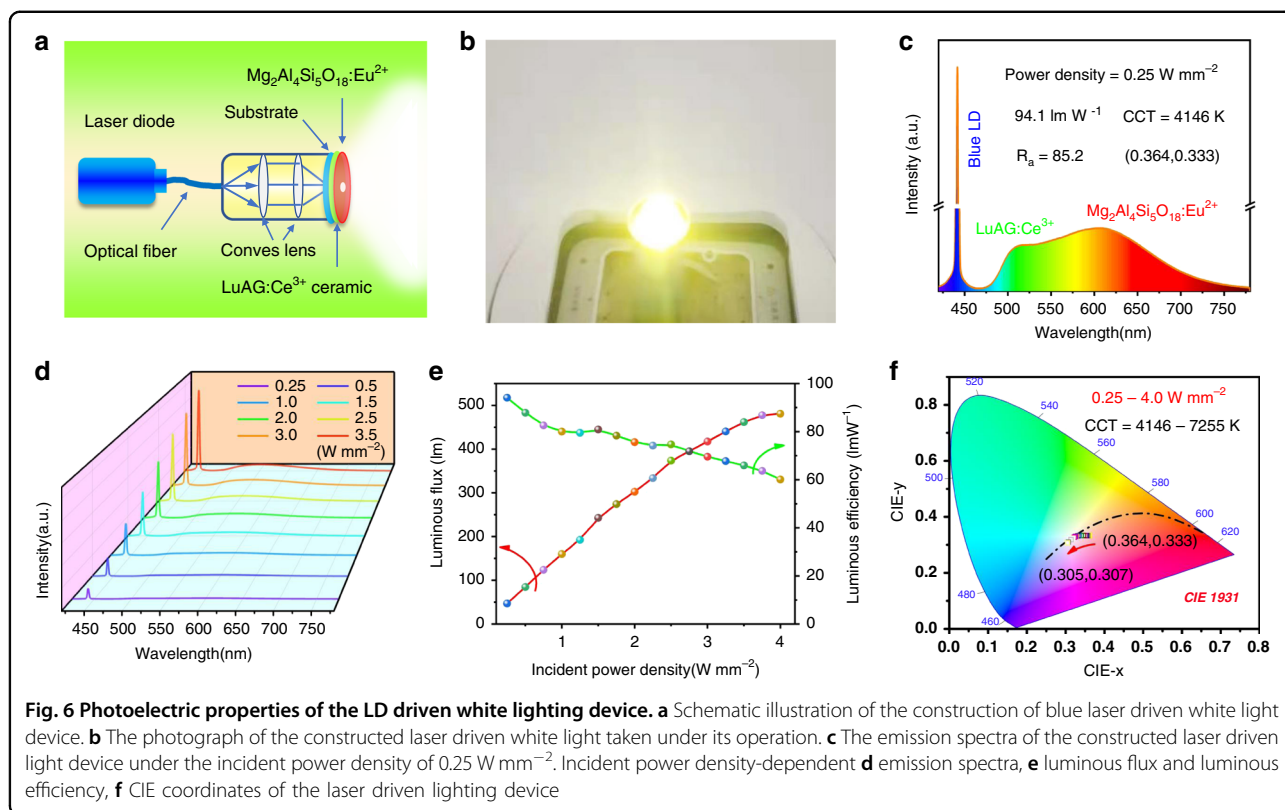
Methods

Materials and preparation

The precursor glass (PG) with nominal composition of $2\text{MgO}-\text{Al}_2\text{O}_3-3\text{SiO}_2$ was prepared via melt-quenching method, and a small amount of Eu_2O_3 was introduced

into the PG to serve as the source of Eu^{2+} dopant. In a detailed preparation procedure, the raw materials of MgO (1.1612 g), Al_2O_3 (2.039 g), SiO_2 (3.605 g), and Eu_2O_3 (optimal doping amount of 0.05 g) were weighted, mixed, and ground thoroughly in an agate mortar. The mixture was transferred into corundum crucible, and then fully melted at $1550 \text{ }^\circ\text{C}$ for 4 h under a reducing atmosphere ($\text{N}_2/\text{H}_2 = 80\%/20\%$) in the tube furnace. The melt was cooled naturally to $750 \text{ }^\circ\text{C}$ in the tube furnace to form PG and further annealed at $750 \text{ }^\circ\text{C}$ for 5 h to relinquish the internal stress. The red-emitting $\text{Mg}_2\text{Al}_4\text{Si}_5\text{O}_{18}:\text{Eu}^{2+}$ bulk composite was prepared via heat treatment of the PG at $1120 \text{ }^\circ\text{C}$ for 15 min under a reducing atmosphere ($\text{N}_2/\text{H}_2 = 80\%/20\%$). However, blue-emitting $\text{Mg}_2\text{Al}_4\text{Si}_5\text{O}_{18}:\text{Eu}^{2+}$ bulk composite can be also prepared by using the same method, while with the different PG composition, $2\text{MgO}-\text{Al}_2\text{O}_3-4\text{SiO}_2$. The obtained PG and composite phosphor were cut and polished before characterizations.

Worthy to mention, the glass melt liquid usually needs to be cooled down at a sufficiently high rate to escape crystallization, so that the liquid melt should be taken out from furnace at high temperature and quenched as fast as possible, which poses extra-cost and dangerous. Commandably, the PG in our case can be fabricated in a more convenient way of melt slowly cooled in the furnace. This added advantage is benefited from a relatively high



viscosity (τ) of silicate melt and a steep increase of viscosity with decreasing temperature (Fig. 1a), leading to large-scale atomic rearrangements are no longer possible.

Characterization

The thermodynamic parameters of the PG were measured by a DTA method on the NETZSCH STA 449C with the heating rate of 10 K min^{-1} . The thermal conductivity was measured on Physical Property Measurement System (ppms-9). The phase identifications were performed by using powder X-ray diffraction, on AERIS X-ray diffractometer operating at 40 kV and 15 mA. Synchrotron XRD pattern for Rietveld analysis was collected at high-resolution powder diffraction end station ($\lambda = 0.82656 \text{ \AA}$, 15 KeV) and MYTHEN 24 K detector. The Eu valance state was examined by Eu L_3 -edge of X-ray absorption near-edge structure spectroscopy in fluorescence mode. The Rietveld refinement was performed by using TOPAS 4.2 software. The SEM image and elemental mapping of the PG were acquired on HITACHI Regulus 8100 scanning electron microscope equipped with an energy-dispersive X-ray spectroscopy (EDS) system. Scanning transmission electron microscopy (STEM) image were taken on a FEI aberration-corrected Titan Cubed S-Twin transmission electron microscope operating in a high-angle annular dark-field (HAADF) mode equipped with an energy dispersive X-ray

spectroscopy operated at 200 kV. High-resolution transmission electron microscopy (HRTEM) image and selected electron diffraction (SAED) were taken on transmission electron microscope (JEOL, JEM-2100 and JEM-2010) operating at 200 kV. A Bruker vector 33 spectrometer is used for the measurement of Fourier-transform infrared (FTIR) spectra. The PL and PLE spectra, quantum efficiency, temperature-dependent PL, and temperature-dependent fluorescent decay curves were all recorded on an Edinburgh Instrument FLS1000 spectrofluorometer equipped with a xenon lamp (450 W) as the excitation source. The photoelectric properties of the red emitting device fabricated by $\text{Mg}_2\text{Al}_4\text{Si}_5\text{O}_{18}:\text{Eu}^{2+}$ composite under the high-power 445 nm blue laser excitation, and the white lighting device fabricated by coupling commercial green-emitting $\text{LuAG}:\text{Ce}^{3+}$ ceramic (purchased from Suzhou Chuangside New Material Co. Ltd) and the $\text{Mg}_2\text{Al}_4\text{Si}_5\text{O}_{18}:\text{Eu}^{2+}$ composite under the high-power 445 nm blue laser excitation were measured using an integrating sphere of 1.0 m in diameter connected to a CCD detector.

Computational methodology

Periodic density functional theory (DFT) calculations on $\text{Mg}_2\text{Al}_4\text{Si}_5\text{O}_{18}:\text{Eu}^{2+}$ were conducted using the Perdew-Burke-Ernzerhof (PBE)⁴⁵ functional and its PBE + U variant with $U_{\text{eff}} = 2.5 \text{ eV}$ for the Eu $4f$ electrons^{46,47}, as

implemented in the Vienna Ab initio Simulation Package (VASP) code^{48,49}. Mg(2p⁶3s²), Al(3s²3p¹), Si(3s²3p⁶), O(2s²2p⁴), and Eu(5s²5p⁶4f⁷6s²) were treated as valence electrons, and their interactions with the respective cores were described by the projected augmented wave approach⁵⁰. The investigation of Eu²⁺-doping in Mg₂Al₄Si₅O₁₈ was modeled by incorporating a Eu in the unit cell (58 atoms), with appropriate charge compensators as described in the text. The atomic structures of undoped and doped supercells were fully optimized until the total energies and the forces on the atoms converged to 10⁻⁶ eV and 0.01 eV Å⁻¹. A 2 × 2 × 2 k-point grid was used, and the cutoff energy for the plane wave basis was set to 530 eV. The formation energies of Eu²⁺-related isolated defects or defect complexes were calculated using $\Delta E_f = E(\text{doped}) - E(\text{undoped}) + \sum \Delta n_A \mu_A$, where $E(\text{doped})$ and $E(\text{undoped})$ denote DFT total energies of the doped and undoped unit cells, respectively. Δn_A is the number of species A (=Eu, Mg, Al, or Si) removed from the undoped cell to introduce point defects, and μ_A is the corresponding atomic chemical potential, which was approximated by the energy of the corresponding metallic atom in view of the fact that the material was prepared in the reducing atmosphere.

Acknowledgements

The present work was supported by the National Natural Science Foundations of China (Grant Nos. 51972118, 51961145101, 51722202 and 11974022), the Guangzhou Science & Technology Project (202007020005), the Fundamental Research Funds for the Central Universities (D2190980), and the Local Innovative and Research Teams Project of Guangdong Pearl River Talents Program (2017BT01X137).

Author details

¹School of Physics and Optoelectronics, State Key Laboratory of Luminescent Materials and Devices and Guangdong Provincial Key Laboratory of Fiber Laser Materials and Applied Techniques, South China University of Technology, Guangzhou, Guangdong, China. ²Anhui Key Laboratory of Optoelectric Materials Science and Technology, Key Laboratory of Functional Molecular Solids, Ministry of Education, Anhui Normal University, Wuhu, Anhui, China. ³School of Applied Physics and Materials, Wuyi University, Jiangmen, Guangdong, China. ⁴Ministry of Education Key Laboratory of Bioinorganic and Synthetic Chemistry, State Key Laboratory of Optoelectronic Materials and Technologies, KLGHEI of Environment and Energy Chemistry, School of Chemistry and Chemical Engineering, Sun Yat-sen University, Guangzhou, Guangdong, China. ⁵Laboratory of Crystal Physics, Kirensky Institute of Physics, Federal Research Center KSC SB RAS, Krasnoyarsk, Russia. ⁶Siberian Federal University, Krasnoyarsk, Russia. ⁷Research and Development Department, Kemerovo State University, Kemerovo, Russia. ⁸Institute of Microstructure and Property of Advanced Materials, Beijing University of Technology Beijing, Beijing, China

Author contributions

H.Z., G.X., and Q.Y.Z. conceived the project, wrote the paper and were primarily responsible for the experiment. L.X.N. performed the DFT calculations and was responsible for discussion of the results. G.Y. carried out photoluminescence measurements. J.W.Q., E.H.S., and Z.T.C. were responsible for discussion of the results. J.W. and Y.Y.Z. helped to fabricate LD devices. M.M. performed the structure refinement. X.X.K. performed the STEM measurement. All authors contributed to the general discussion.

Conflict of interest

The authors declare no competing interests.

Supplementary information The online version contains supplementary material available at <https://doi.org/10.1038/s41377-021-00498-6>.

Received: 17 January 2021 Revised: 9 February 2021 Accepted: 24 February 2021

Published online: 12 March 2021

References

- Pust, P., Schmidt, P. J. & Schnick, W. A revolution in lighting. *Nat. Mater.* **14**, 454–458 (2015).
- Pimpitkar, S. et al. Prospects for LED lighting. *Nat. Photonics* **3**, 180–182 (2009).
- Schubert, E. F. & Kim, J. K. Solid-state light sources getting smart. *Science* **308**, 1274–1278 (2005).
- Xia, Z. G. & Liu, Q. L. Progress in discovery and structural design of color conversion phosphors for LEDs. *Prog. Mater. Sci.* **84**, 59–117 (2016).
- Kim, Y. H. et al. A zero-thermal-quenching phosphor. *Nat. Mater.* **16**, 543–550 (2017).
- Pust, P. et al. Narrow-band red-emitting Sr[LiAl₃N₄]:Eu²⁺ as a next-generation LED-phosphor material. *Nat. Mater.* **13**, 891–896 (2014).
- Zhao, M. et al. Next-generation narrow-band green-emitting RbLi(Li₃SiO₄)₂:Eu²⁺ phosphor for backlight display application. *Adv. Mater.* **30**, 1802489 (2018).
- Wierer, J. J. Jr, Tsao, J. Y. & Sizov, D. S. Comparison between blue lasers and light-emitting diodes for future solid-state lighting. *Laser Photonics Rev.* **7**, 963–993 (2013).
- Cho, J., Schubert, E. F. & Kim, J. K. Efficiency droop in light-emitting diodes: challenges and countermeasures. *Laser Photonics Rev.* **7**, 408–421 (2013).
- Neuf, A. et al. Phosphor performance under high intensity excitation by InGaN laser diodes. *ECS J. Solid State Sci. Technol.* **9**, 016019 (2019).
- Li, S. X. et al. Color conversion materials for high-brightness laser-driven solid-state lighting. *Laser Photonics Rev.* **12**, 1800173 (2018).
- Huang, J. L. et al. Rapid degradation of mid-power white-light LEDs in saturated moisture conditions. *IEEE Trans. Device Mater. Reliab.* **15**, 478–485 (2015).
- Lin, H. et al. Glass ceramic phosphors: towards long-lifetime high-power white light-emitting-diode applications—a review. *Laser Photonics Rev.* **12**, 1700344 (2018).
- Arjoca, S. et al. Temperature dependence of Ce:YAG single-crystal phosphors for high-brightness white LEDs/LDs. *Mater. Res. Express* **2**, 055503 (2015).
- Yao, Q. et al. YAG:Ce³⁺ transparent ceramic phosphors brighten the next-generation laser-driven lighting. *Adv. Mater.* **32**, 1907888 (2020).
- Zhang, R. et al. A new-generation color converter for high-power white LED: transparent Ce³⁺:YAG phosphor-in-glass. *Laser Photonics Rev.* **8**, 158–164 (2014).
- Zhang, D. et al. Highly efficient phosphor-glass composites by pressureless sintering. *Nat. Commun.* **11**, 2805 (2020).
- Huang, P. et al. Nano wave plates structuring and index matching in transparent hydroxyapatite-YAG: Ce composite ceramics for high luminous efficiency white light-emitting diodes. *Adv. Mater.* **32**, 1905951 (2020).
- Hoerder, G. J. et al. Sr[Li₂Al₂O₇N₂]:Eu²⁺—A high performance red phosphor to brighten the future. *Nat. Commun.* **10**, 1824 (2019).
- Qiao, J. W. et al. Site-selective occupancy of Eu²⁺ toward blue-light-excited red emission in a Rb₃YSi₂O₇:Eu phosphor. *Angew. Chem. Int. Ed.* **58**, 11521–11526 (2019).
- Wang, R. et al. Red-emitting improvement of CaAlSiN₃:Eu²⁺ phosphor-in-glass: insight into the effect of atmospheric pressure preparation on photoluminescence properties and thermal degradation. *J. Lumin.* **225**, 117390 (2020).
- Li, S. X. et al. New insights into the microstructure of translucent CaAlSiN₃:Eu²⁺ phosphor ceramics for solid-state laser lighting. *J. Mater. Chem. C* **4**, 1042–1051 (2017).
- Allix, M. et al. Highly transparent BaAl₄O₇ polycrystalline ceramic obtained by full crystallization from glass. *Adv. Mater.* **24**, 5570–5575 (2012).
- Alahraché, S. et al. Crystallization of Y₂O₃-Al₂O₃ rich glasses: synthesis of YAG glass-ceramics. *J. Phys. Chem. C* **115**, 20499–20506 (2011).
- Ma, X. G. et al. Pressureless glass crystallization of transparent yttrium aluminum garnet-based nanoceramics. *Nat. Commun.* **9**, 1175 (2018).
- Zhou, S. F. et al. Simultaneous tailoring of phase evolution and dopant distribution in the glassy phase for controllable luminescence. *J. Am. Chem. Soc.* **132**, 17945–17952 (2010).

27. Chen, D. Q. et al. Simultaneous tailoring of dual-phase fluoride precipitation and dopant distribution in glass to control upconverting luminescence. *ACS Appl. Mater. Interfaces* **11**, 30053–30064 (2019).
28. Chowdhury, A. et al. Synthesis, properties and applications of cordierite ceramics, Part 1. *Int. Ceram. Rev.* **56**, 18–22 (2007).
29. Chen, J. et al. The luminescence properties of novel α - $\text{Mg}_2\text{Al}_4\text{Si}_5\text{O}_{18}:\text{Eu}^{2+}$ phosphor prepared in air. *RSC Adv.* **4**, 18234–18239 (2014).
30. Zhou, J. et al. New insight into phase formation of $\text{M}_x\text{Mg}_2\text{Al}_{4+x}\text{Si}_{5-x}\text{O}_{18}:\text{Eu}^{2+}$ solid solution phosphors and its luminescence properties. *Sci. Rep.* **5**, 12149 (2015).
31. Song, K. et al. Synthesis and luminescence characteristics of $\text{Mg}_2\text{Al}_4\text{Si}_5\text{O}_{18}:\text{Eu}^{2+}$ and nitrided $\text{Mg}_2\text{Al}_4\text{Si}_5\text{O}_{18}:\text{Eu}^{2+}$ phosphors. *J. Lumin.* **224**, 117317 (2020).
32. Stefańska, D. & Dereń, P. J. High efficiency emission of Eu^{2+} located in channel and Mg-site of $\text{Mg}_2\text{Al}_4\text{Si}_5\text{O}_{18}$ cordierite and its potential as a Bi-functional phosphor toward optical thermometer and white LED application. *Adv. Optical Mater.* **8**, 2001143 (2020).
33. Komatsu, T. Design and control of crystallization in oxide glasses. *J. Non-Cryst. Solids* **428**, 156–175 (2015).
34. Höland, W. & Beall, G. H. *Glass-Ceramic Technology* 2nd edn (Wiley, 2012).
35. Bruker, A. X. S. *TOPAS, V4: General Profile and Structure Analysis Software for Powder Diffraction Data-User's Manual* (Bruker AXS, 2008).
36. Clayden, N. J. et al. Solid state ^{27}Al NMR and FTIR study of lanthanum aluminosilicate glasses. *J. Non-Cryst. Solids* **258**, 11–19 (1999).
37. Mozgawa, W. & Sitarz, M. Vibrational spectra of aluminosilicate ring structures. *J. Mol. Struct.* **614**, 273–279 (2002).
38. Hume-Rothery, W. & Powell, H. M. On the theory of super-lattice structures in alloys. *Z. für. Kristallographie* **91**, 23–47 (1935).
39. Thomas, P. et al. Powder neutron diffraction study of alkali-substituted cordierites with $\text{M}_x\text{Mg}_2\text{Al}_{4+x}\text{Si}_{5-x}\text{O}_{18}$ ($\text{M} = \text{K}, \text{Cs}; 0 < x \leq 1$) formula. *Eur. J. Solid State Inorg. Chem.* **28**, 1011–1120 (1991).
40. Grau-Crespo, R. et al. Symmetry-adapted configurational modelling of fractional site occupancy in solids. *J. Phys. Condens. Matter* **19**, 256201 (2007).
41. Poort, S. H. M., Meyerink, A. & Blasse, G. Lifetime measurements in Eu^{2+} -doped host lattices. *J. Phys. Chem. Solids* **58**, 1451–1456 (1997).
42. Dorenbos, P. Thermal quenching of Eu^{2+} 5d-4f luminescence in inorganic compounds. *J. Phys. Condens. Matter* **17**, 8103 (2005).
43. Qiao, J. W. et al. Eu^{2+} site preferences in the mixed cation $\text{K}_2\text{BaCa}(\text{PO}_3)_2$ and thermally stable luminescence. *J. Am. Chem. Soc.* **140**, 9730–9736 (2018).
44. Dorenbos, P. Anomalous luminescence of Eu^{2+} and Yb^{2+} in inorganic compounds. *J. Phys. Condens. Matter* **15**, 2645 (2003).
45. Perdew, J. P., Burke, K. & Ernzerhof, M. Generalized gradient approximation made simple. *Phys. Rev. Lett.* **77**, 3865–3868 (1996).
46. Canning, A. et al. First-principles study of luminescence in Ce-doped inorganic scintillators. *Phys. Rev. B* **83**, 125115 (2011).
47. Dudarev, S. L. et al. Electron-energy-loss spectra and the structural stability of nickel oxide: an LSDA + U study. *Phys. Rev. B* **57**, 1505–1509 (1998).
48. Kresse, G. & Furthmüller, J. Efficient iterative schemes for ab initio total-energy calculations using a plane-wave basis set. *Phys. Rev. B* **54**, 11169–11186 (1996).
49. Kresse, G. & Joubert, D. From ultrasoft pseudopotentials to the projector augmented-wave method. *Phys. Rev. B* **59**, 1758–1775 (1999).
50. Blöchl, P. E. Projector augmented-wave method. *Phys. Rev. B* **50**, 17953–17979 (1994).